

Article

Seismic Fragility Assessment of Cable-Stayed Bridges Crossing Fault Rupture Zones

Junjun Guo ¹, Yitong Gu ¹, Weihong Wu ², Shihyu Chu ³ and Xinzhi Dang ^{1,*}

¹ State Key Laboratory of Disaster Reduction in Civil Engineering, Tongji University, 1239 Siping Road, Shanghai 200092, China; guojj@tongji.edu.cn (J.G.); guyitong@tongji.edu.cn (Y.G.)

² Gansu Transportation Planning Survey and Design Institute Co., Ltd., Lanzhou 730010, China; wwh_3040@163.com

³ Department of Civil Engineering, National Cheng Kung University, No. 1 University Road, Tainan 701, Taiwan; sychu@mail.ncku.edu.tw

* Correspondence: 021tjdangxz@tongji.edu.cn

Abstract: Current studies lack probabilistic evaluations on the performance of fault-crossing bridges. This paper conducts seismic fragility analyses to evaluate the fragility of cable-stayed bridges with the effects of fault ruptures. Synthetic across-fault ground motions are generated using existing simulation methods for the low-frequency pulses and high-frequency residuals. Incremental dynamic analysis is utilized to generate the seismic responses of the bridge. The optimal intensity measure (IM) for a cable-stayed bridge that crosses a fault is identified based on the coefficient of determination (R^2). Root-mean-square velocity (V_{rms}) is found to be the best IM for cable-stayed bridges traversed by fault ruptures, instead of the commonly used ones such as peak ground acceleration or velocity (PGA or PGV). Fragility curves for the critical components of fault-crossing cable-stayed bridges, including pylons, cables, and bearings, are developed using the IM of V_{rms} , and are subsequently compared with those for the cable-stayed bridge near faults. Results show that the bearings on transition piers are the most vulnerable component for fault-crossing cable-stayed bridges because of the rotation of their girder. Compared to cable-stayed bridges near faults, pylons and bearings are more vulnerable in the transverse direction for cable-stayed bridges crossing faults, whereas the vulnerability of cables is comparable.

Keywords: cable-stayed bridge; crossing faults; synthetic ground motions; intensity measure; fragility analysis



Citation: Guo, J.; Gu, Y.; Wu, W.; Chu, S.; Dang, X. Seismic Fragility Assessment of Cable-Stayed Bridges Crossing Fault Rupture Zones.

Buildings **2022**, *12*, 1045. <https://doi.org/10.3390/buildings12071045>

Academic Editor: Antonio Formisano

Received: 24 June 2022

Accepted: 14 July 2022

Published: 19 July 2022

Publisher's Note: MDPI stays neutral with regard to jurisdictional claims in published maps and institutional affiliations.



Copyright: © 2022 by the authors. Licensee MDPI, Basel, Switzerland. This article is an open access article distributed under the terms and conditions of the Creative Commons Attribution (CC BY) license (<https://creativecommons.org/licenses/by/4.0/>).

1. Introduction

The large velocity pulse and large ground displacement in near-fault regions usually lead to significant damage to bridges traversed by fault ruptures. These two devastating effects, known as “forward directivity” and “fling-step”, have been shown in previous earthquakes [1,2]. In order to avoid bridges suffering from undesirable calamities, many seismic design codes recommend preventing the construction of bridges that traverse crossing faults. However, it is sometimes inevitable to construct fault-crossing bridges [2,3]. As a result, it is crucial to study the seismic behavior of bridges crossing fault ruptures.

Although considerable research has been conducted on the seismic performance of fault-crossing girder bridges [3–11], there is limited research on evaluating the responses of fault-crossing long-span bridges [12,13]. Zeng et al. [14] studied the seismic responses of a cable-stayed bridge, and they found that the magnitude of the permanent ground displacement can significantly affect the bridge's responses. Gu et al. [15] evaluated the seismic responses of cable-stayed bridges that cross faults. However, most of the previous studies on fault-crossing bridges utilize a deterministic method with a few ground motions as the input, and thus cannot account for the uncertainties of both bridges and earthquakes.

A major challenge that limits scholars from probabilistic analyses on fault-crossing bridges is the lack of actual motions recorded on both sides of the fault rupture. Researchers have made great efforts to address this issue. Generally, the approaches to obtaining ground motions with distinct characteristics of pulse-like earthquakes can be divided into two categories: (1) performing baseline corrections to raw records and (2) generating ground motions using numerical models.

For the first approach, the main objective is to preserve the permanent ground static offset from actual records. Wu et al. [16] developed an improved baseline correction method by modifying the models proposed by Iwan [17] and Boore [18]. The improved method is applied to the Chichi and Chengkung earthquake data to compute the coseismic displacements, and the results show favorable agreement with GPS measurements. Lin et al. [19] proposed a new baseline correction scheme to obtain ground motions with target final displacements. By considering six simulated fling-step ground motions, Zhang et al. [11] studied the seismic behavior of girder bridges crossing faults.

For the second approach, the main objective is to build an artificial across-fault ground motion with directivity or fling pulse. Various researchers have proposed low-frequency pulse models. Menun [20] developed an analytical model defined by five parameters for ground motions in the fault-normal (FN) direction. Mavroeidis et al. [21] introduced a mathematical model and calibrated that the model can capture the characteristics of near-fault motions. Makris et al. [22] demonstrated that a one-cosine acceleration pulse causes the velocity pulse. Hoseini Vaez et al. [23] presented a new model to simulate the velocity pulses. Kamai et al. [24] simulated the velocity pulses with a half-period sine wave. Burks et al. [25] defined the fault-parallel (FP) fling by a ramp function and derived a predictive model for the parameters. Yadav et al. [26] modeled the fling-step velocity pulse using a function related to the pulse's amplitude, duration, and location. Hamidid et al. [27] used the Green function to simulate the ground motions. In particular, the model proposed by Mavroeidis et al. [21] successfully simulates the FN and FP pulses of the ground motion across a strike-slip fault [28]. In addition to the low-frequency pulse models, the specific barrier model [29] and stochastic model [30–34] are proposed to represent the high-frequency content of the motions.

Since various numerical models have been developed so far, it is possible to investigate fault-crossing bridges with probabilistic seismic-risk assessment approaches. Developing structure fragility curves is one practical and effective tool for probabilistic seismic-risk assessments. In the past two decades, much research has been carried out to evaluate the vulnerability of bridges. However, most previous studies focused on girder bridges. Pang et al. [35] performed a vulnerability analysis of cable-stayed bridges considering various uncertainties. Zhong et al. [13,36–38] studied cable-stayed bridges' fragility in selecting optimal intensity measures and the effect of spatially distributed motions. Wu et al. [39] conducted the fragility of a concrete cable-stayed bridge subjected to far-field motions. Wang et al. [40] utilized the vulnerability to estimate the effect of an innovative bearing on the performance of a cable-stayed bridge subjected to ground motions with velocity pulses. The fragility curves are established using the incremental dynamic analyses (IDA) method. Li et al. [41] assessed the fragility of a cable-stayed bridge adopting synthetic offshore multi-support ground motions. Wei et al. [42] conducted seismic fragility analysis of a multipylon cable-stayed bridge with super-high piers. Nevertheless, fragility assessments for fault-crossing cable-stayed bridges are still insufficient.

This study aims to conduct the fragility assessment of cable-stayed bridge crossing faults. First, using the existing mathematical models, fling-step motions are simulated by superimposing the long-period pulses and their high-frequency residuals. Then, a numerical model is constructed with the OpenSeesPy platform [43]. The synthetic ground motions are adopted as inputs to perform nonlinear analysis. Subsequently, the appropriate intensity measure is selected for cable-stayed bridges crossing faults, and the fragility curves are developed. Moreover, the vulnerability of cable-stayed bridges subjected to

fling-step and velocity pulse motions are compared. Finally, several conclusions of this study are presented.

2. Seismic Fragility Methodology

Seismic fragility is a conditional probability that gives a bridge's likelihood to meet or exceed a certain level of damage for a given intensity measure (IM) [44]. Assuming both the demand (D) and capacity (C) follow lognormal distributions, the fragility function can be represented as follows:

$$P = P[D \geq C | IM] = \Phi \left[\frac{\ln(D) - \ln(C)}{\sqrt{\beta_D^2 + \beta_C^2}} \right] \quad (1)$$

where D and C are the mean values of demand and capacity, respectively; β_D and β_C are the logarithmic standard deviations, and $\Phi[\cdot]$ is the standard normal cumulative distribution function.

To develop the fragility curves, it is necessary to obtain the demand (D) beforehand. D is estimated using a probabilistic seismic-demand model (PSDM) in fragility analysis. PSDM expresses the relationship between the demand D and the IM. Conventionally, D and IM are assumed to exhibit a linear regression relationship in the logarithmic space as:

$$\ln(D) = a \ln(IM) + b \quad (2)$$

where a and b are regression coefficients. Alternatively, Pan et al. [45] apply a quadratic regression to fit the data. Zhong et al. [13] used quadratic regression to obtain the PSDM for a cable-stayed bridge. The quadratic PSDM takes the form:

$$\ln(D) = a \ln^2(IM) + b \ln(IM) + c \quad (3)$$

where a , b , and c are the regression coefficients. Thus, once the damage state and component capacity S_C are determined, the fragility curve can be derived by using Equation (1).

3. Simulation of the Ground Motions

This study generates synthetic across-fault ground motions by combining the simulated coherent (long-period) and incoherent (high-frequency) components. Specifically, the high-frequency components in horizontal directions (FN and FP directions) are simulated with a stochastic model proposed by Dabaghi et al. [32–34], whereas the long-period components are simulated according to the pulse model proposed by Mavroeidis et al. [21]

3.1. Ground-Motion Models

Dabaghi et al. [32] pointed out that the residual of a velocity pulse motion after removal of the pulse is generally a broadband time series. A model proposed by Rezaeian et al. [30,31] and adopted by Dabaghi et al. [32–34] can be used to describe these broadband motions. The expression of this MFW model is:

$$a_{\text{MFW}} = q(t) \left\{ \frac{1}{\sigma_h(t)} \int_{-\infty}^t h[t - \tau, \lambda(\tau)] w(\tau) d\tau \right\} \quad (4)$$

where $w(t)$ is a white-noise process, $\sigma_h(t)$ is the standard deviation of the process defined by the integral, $q(t)$ is a time-modulating function that characterizes the root-mean-square of the acceleration process, and $h[t - \tau, \lambda(\tau)]$ is the unit-impulse response function (IRF) of a linear filter with the time-varying parameter $\lambda(\tau) = [\omega_f(\tau), \zeta_f(\tau)]$, given as follows:

$$h[t - \tau, \lambda(\tau)] = \begin{cases} \frac{\omega_f(\tau)}{\sqrt{1 - \zeta_f^2(\tau)}} e^{-\zeta_f(\tau) \omega_f(\tau)(t - \tau)} \sin \left[\omega_f(\tau) \sqrt{1 - \zeta_f^2(\tau)} (t - \tau) \right], & \tau \leq t \\ 0, & \text{elsewhere} \end{cases} \quad (5)$$

where τ is the time of the pulse, $\zeta_f(\tau)$ is the filter damping that represents the bandwidth of the acceleration process (regarded as a constant), and $\omega_f(\tau)$ is the filter frequency:

$$\omega_f(\tau) = 2\pi [f_{\text{mid}} + f'(\tau - t_{\text{mid}})] \quad (6)$$

where f_{mid} is the filter frequency at the middle of the motion t_{mid} , and f' is the frequency change rate with time.

For the modulating function $q(t)$, a four-parameter piecewise function is presented as:

$$q(t) = \begin{cases} 0, & t \leq t_{0,q} \\ c \left(\frac{t-t_{0,q}}{t_{\text{max},q}-t_{0,q}} \right)^{\alpha}, & t_{0,q} < t \leq t_{\text{max},q} \\ ce^{-\beta(t-t_{\text{max},q})}, & t_{\text{max},q} < t \end{cases} \quad (7)$$

where $t_{0,q}$ is the starting time, $t_{\text{max},q}$ is the time that the modulating function arrives at its peak, α is the order of the polynomial at the start of the function, β is the decaying rate of an exponential function in the end phase of the function, and c controls the amplitude of the modulating function. These four parameters ($t_{\text{max},q}$, α , β , c) are related to the Arias intensity of the motion.

The model put forward by Mavroeidis et al. [21] (M03 model) has been widely employed for generating the long-period pulse of near-fault motions. Currently, when simulating the fling of the motion, the M03 model is adopted with its original form as follows:

$$v_{\text{pul}}(t) = \begin{cases} \frac{V_p}{2} \left[1 + \cos\left(\frac{2\pi}{\gamma T_p}(t-t_0)\right) \right] \cos\left[\frac{2\pi}{T_p}(t-t_0)+v\right], & t_0 - \frac{\gamma}{2}T_p < t \leq t_0 + \frac{\gamma}{2}T_p \\ 0, & \text{otherwise} \end{cases} \quad (8)$$

where V_p is the pulse magnitude, T_p is the period, γ is a variable controlling the oscillation number of a pulse, v is the phase angle, and t_0 is the epoch of the peak of the envelope.

For the simulation of the velocity pulse, the form of the MP model proposed by Dabaghi et al. [32] is adopted:

$$v_{\text{pul}}(t) = \begin{cases} \left\{ \frac{V_p}{2} \cos\left[2\pi\left(\frac{t-t_{\text{max},p}}{T_p}\right)+v\right] - \frac{D_r}{\gamma T_p} \right\} \left\{ 1 + \cos\left[\frac{2\pi}{\gamma}\left(\frac{t-t_{\text{max},p}}{T_p}\right)\right] \right\}, & t_{\text{max},p} - \frac{\gamma}{2}T_p < t \leq t_{\text{max},p} + \frac{\gamma}{2}T_p \\ 0, & \text{elsewhere} \end{cases} \quad (9)$$

where t_0 in Equation (8) is replaced by $t_{\text{max},p}$, and D_r is a permanent displacement represented with $D_r = V_p T_p \frac{\sin(v+\gamma\pi) - \sin(v-\gamma\pi)}{4\pi(1-\gamma^2)}$.

Additionally, the FN component of the simulated motions is checked, adopting the criteria put forward by Baker [46] to ensure that it contains a velocity pulse. The three criteria can be found in [46] and are given here for convenience:

- (1) The equation of the pulse indicator (larger than 0.85) is given as:

$$\text{Pulse indicator} = \frac{1}{1 + e^{-23.3+14.6(\text{PGV ratio})+20.5(\text{energy ratio})}}$$

where the PGV ratio is defined as the PGV of the residual record divided by the original record's PGV and the energy ratio with a similar definition.

- (2) The pulse occurs at the early stage of the motion, as indicated by the time when the original record reaches 20% of its total cumulative squared velocity (CSV) and is greater than the time at which the pulse reaches 10% of its CSV.
- (3) The PGV of the motion is larger than 30 cm/s.

3.2. Determination of the Input Parameters of the Models

Input parameters of the models for high-frequency components and the forward-directivity pulse are determined through linear predictive equations developed by

Dabaghi et al. [32–34], according to the source and site characteristics. Specifically, seven parameters are selected for the predictive equations, including the type of faulting (F), the moment magnitude (M), the depth to the top of the rupture plane (Z_{TOR}), the closest distance from the site to the fault rupture (R_{RUP}), the shear-wave velocity of the top 30 m of soil at the site (V_{s30}), and directivity parameters s (or d) and θ (or φ). The schematic of the directivity parameters is plotted in Figure 1. Detailed procedures for the regression of these model parameters can be found in [32–34].

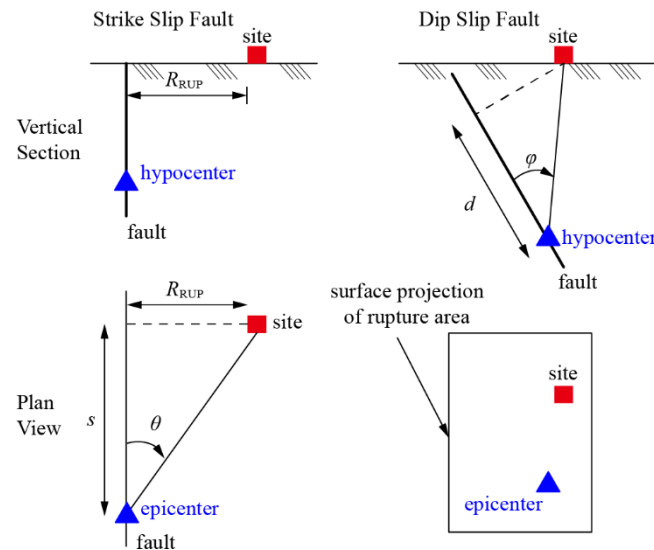


Figure 1. Directivity parameters [47].

Input parameters of the fling model are determined following the guidelines recommended by Yang et al. [28]. It is noteworthy that choosing equations for estimating the parameters for the fling model is not unique. In this study, the predictive equations proposed by Abrahamson [48] are selected.

Table 1 lists the predictive equations for estimating the input parameters.

Table 1. Predictive equations for the input parameters.

Model	Predictive Equation	Reference
MFW model	$\alpha, \beta, c, t_{\max,q}, f_{\text{mid}}, f' = \mathbf{F}(F, M, Z_{TOR}, R_{RUP}, V_{s30}, s, \theta)$ $t_{0,q} = 0$	[32–34]
Directivity pulse model	$V_p, T_p, \gamma, \nu, t_{\max,p} = \mathbf{F}(F, M, Z_{TOR}, R_{RUP}, V_{s30}, s, \theta)$	[32–34]
Fling model	$V_p = 2D_{\text{site}}/[T_p/(2 + \varepsilon)], \varepsilon \in (0,0.1]$ $\log(T_p) = \log(2 + \varepsilon) - 3.00 + 0.50M, \varepsilon \in (0,0.1]$ $\log(D_{\text{site}})_{\text{avg}} = -1.70 + 0.50M,$ $(D_{\text{site}})_{\text{max}} \approx (D_{\text{site}})_{\text{avg}}/\lambda, \lambda \in [0.2,0.8]$ $\gamma = 1 + \varepsilon, \varepsilon \in (0,0.1]$ $\nu \approx 0 \text{ or } \pi$ $t_0 \geq \gamma T_p/2$	[28]

$(D_{\text{site}})_{\text{max}}$ is used to estimate V_p .

4. Vulnerability Analysis of a Fault-Crossing Bridge

4.1. Depiction of the Analysis Model

A typical cable-stayed bridge is selected as the case study bridge. The bridge has a length of 174 + 352 + 174 m. There are 168 stay cables, whose tensile strength is 1670 MPa, with a fan-typed configuration. The cable force is optimized based on the method proposed by Guo et al. [49].

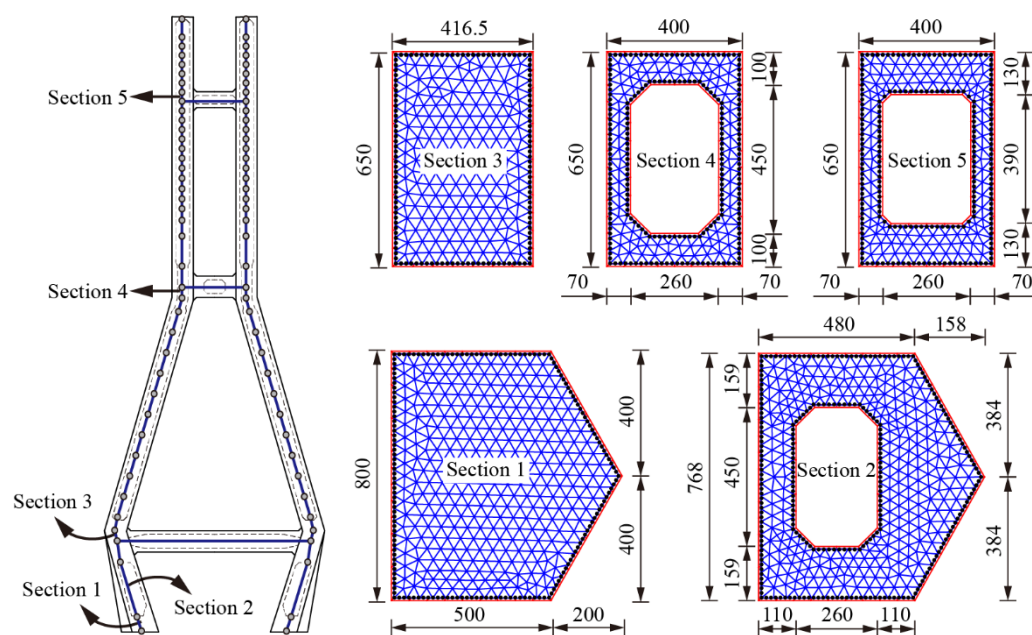


Figure 4. Fiber sections of the pylon (unit: cm).

Material uncertainties are considered for the numerical model of the bridge. In addition, the uncertainty of the actual initial cable forces due to the construction error is also considered. In this study, the compressive strength of the concrete (f_c), yield strength of the rebar (f_y), initial stiffness of the rebar (E), the ratio between the post-yield and initial stiffness, and the ratio between actual and designed initial cable forces (R) are modeled as random variables. Table 2 summarizes the statistical information of these uncertainty parameters.

Table 2. Uncertainty parameters of the bridge and their probability distribution.

Variable	Distribution *	Reference
$f_{c,pylon}$	Normal (C50, $\mu = 32.35$ MPa, $cov = 0.18$)	[50]
$f_{c,pier}$	Normal (C40, $\mu = 26.75$ MPa, $cov = 0.18$)	[50]
f_y	Lognormal (HRB400, $\mu = 400$ MPa, $cov = 0.08$)	[51]
E	Lognormal ($\mu = 2 \times 10^8$ MPa, $cov = 0.033$)	[52]
b	Lognormal ($\mu = 0.005$, $cov = 0.2$)	[35,52]
R	Uniform ($\mu = 1$, $\sigma = 0.1$)	/

* μ denotes the mean; cov denotes the coefficient of variation; σ denotes the standard deviation.

4.2. Ground Motions

It is pointed out that the model developed by Dabaghi et al. should be used within the boundaries of the database, which are $6 \leq M \leq 7.5$, $5 < R_{RUP} \leq 25$ km, and $400 < V_{s30} < 1000$ m/s [32]. Therefore, 25 ground-motion pairs (in FN and FP directions) are simulated with their input parameters randomly generated within the corresponding ranges. It is worth noting that for strike-slip faults, R_{RUP} , s , and θ are correlated with $R_{RUP} = \tan\theta$ if a straight line can represent the rupture and if the site is located alongside the rupture, as shown in Figure 1. In the present study, only the case of vertical strike-slip faults with surface rupture is considered, and the site is assumed to be perpendicular to the epicenter. As a result, F , Z_{TOR} , s , and θ are constrained as 0, 0, 0, and 90° , respectively, in the simulation. Models of the low-frequency pulses and high-frequency residuals are programmed in Python language. Figure 5 presents the time histories of one of the synthetic motions. The “forward-directivity” pulse in the FN direction and the “fling-step” pulse in the FP direction can be successfully simulated. The random parameters of the 25 synthetic ground-motion pairs are listed in Table 3.

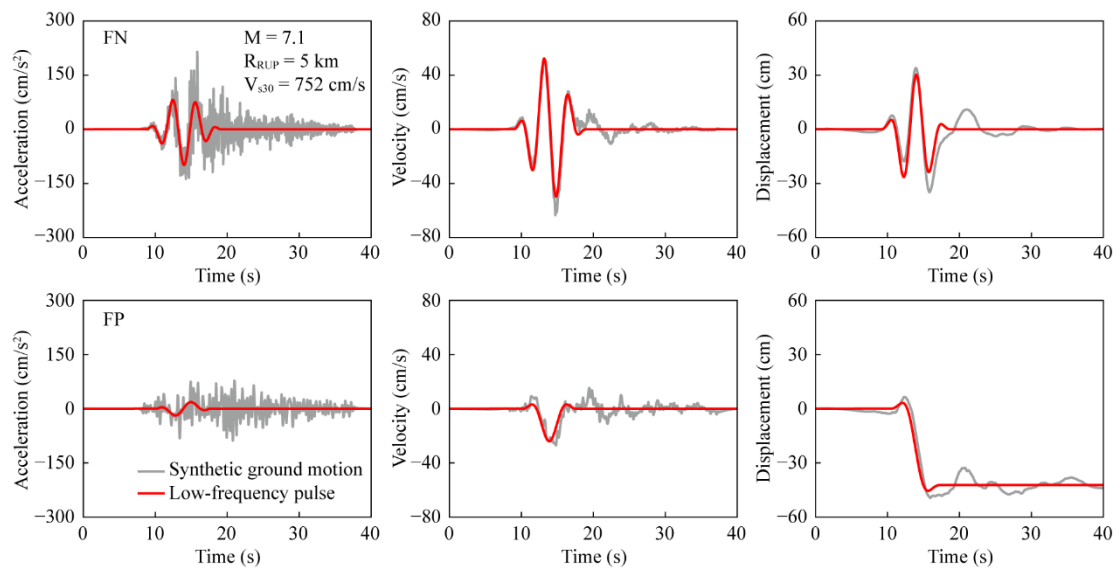


Figure 5. Time histories of a synthetic ground-motion pair.

Table 3. Input parameters of the synthetic ground motions.

GM	M	R_{RUP} (km)	V_{s30} (m/s)	GM	M	R_{RUP} (km)	V_{s30} (m/s)
1	6	10	702	14	7.3	5.1	873
2	7	18.9	446	15	7.2	6.5	508
3	7.1	5	752	16	7.2	8.2	524
4	6.7	15.1	642	17	7	7.9	691
5	7.3	7.8	993	18	6.7	9	651
6	7.1	5.8	954	19	7.5	23.4	445
7	6.3	14.2	691	20	6	15.9	588
8	6.9	8.2	846	21	6.7	10.8	630
9	7.1	20.3	882	22	7.1	8.2	675
10	6.1	7	542	23	6.3	14.3	947
11	7.3	7.2	622	24	6.9	5.8	455
12	6.2	12.4	905	25	6.9	15.1	587
13	6.8	5.9	903				

$F = 0$ for strike-slip faults; $Z_{TOR} = 0$; $s = 0$; $\theta = 90^\circ$.

The synthetic motion pairs are then scaled using a factor ranging from 0.5 to 3 with an increment of 0.5. Thus, 150 ground-motion pairs are generated for the nonlinear time-history analysis. Figure 6 presents the spectra displacement of the input ground motions in FN and FP directions. It shows that the component in the FP direction has larger displacements than that in the FN direction in the long-period range.

According to previous studies, cable-stayed bridges are suggested to cross the fault perpendicularly [15]. Therefore, in this study, the fault rupture should cross the bridge in its middle span with an angle of 90° . The time-history series applies to the bridge supports in the FN and FP directions. Because this study focuses on the vertical strike-slip scenario, the ground dislocation is assumed to distribute equally at the two sides of the fault. As a result, the FN ground motions are the same on each fault side, whereas the FP ground motions have equal amplitudes but with reversed polarity [53] (as shown in Figure 7). To exclude the interference of the effect of vertical ground motions and mainly consider the effect of the FN and FP components, the vertical motions are not considered in this study. The wave passage effect is not considered as well.

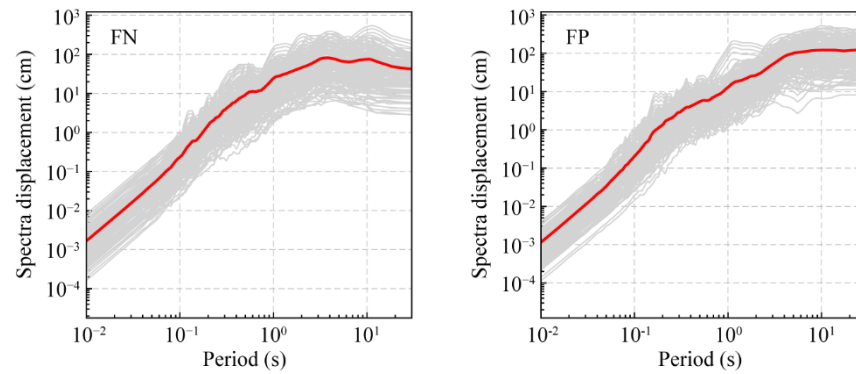


Figure 6. Response spectra of the 150 ground motions.

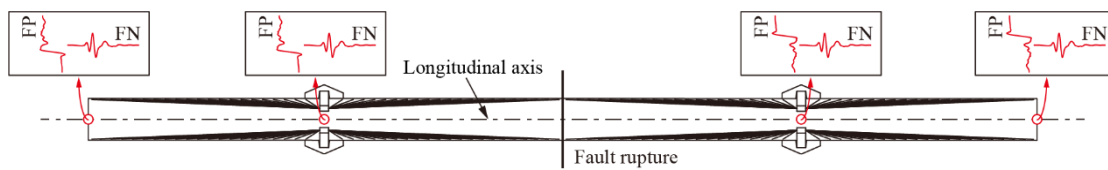


Figure 7. Input ground motions for cable-stayed bridges crossing faults.

4.3. Optimal IM Determination and PSDMs Establishment

The selection of optimal IMs is essential for establishing reliable PSDMs. In this study, 12 IM candidates are examined to identify the optimal one for the fault-crossing cable-stayed bridge. Table 4 gives the definitions of the studied IMs. The IMs are divided into three groups: acceleration-related, velocity-related, and displacement-related. Note that only structure-independent IMs are used in the current study.

Table 4. Description of the considered IMs.

Type	IM	Definition	Reference
Acceleration-related	PGA	Peak ground acceleration $\text{Max} a(t) $, $a(t)$ is the acceleration time history	/
	SMA	Sustained maximum acceleration third largest peak in $a(t)$	[54]
	CAV	Cumulative absolute velocity $\int_0^{t_{\text{tot}}} a(t) dt$, t_{tot} is the total duration	[55]
	I_a	Arias intensity $\frac{\pi}{2g} \int_0^{t_{\text{tot}}} a^2(t) dt$	[56]
	A_{rms}	Root-mean-square of acceleration $\sqrt{\frac{1}{t_{\text{tot}}} \int_0^{t_{\text{tot}}} a^2(t) dt}$	/
Velocity-related	PGV	Peak ground velocity $\text{Max} v(t) $, $v(t)$ is the velocity-time history	/
	SMV	Sustained maximum acceleration third largest peak in $v(t)$	[54]
	CAD	Cumulative absolute displacement $\int_0^{t_{\text{tot}}} v(t) dt$, t_{tot} is the total duration	[55]
	V_{rms}	Root-mean-square of velocity $\sqrt{\frac{1}{t_{\text{tot}}} \int_0^{t_{\text{tot}}} v^2(t) dt}$	/
	I_v	Velocity intensity $\frac{\pi}{2g} \int_0^{t_{\text{tot}}} v^2(t) dt$	[57]
Displacement-related	PGD	Peak ground displacement $\text{Max} d(t) $, $d(t)$ is the displacement-time history	/
	D_{rms}	Root-mean-square of displacement $\sqrt{\frac{1}{t_{\text{tot}}} \int_0^{t_{\text{tot}}} d^2(t) dt}$	/

The geometric mean of the IMs for the FN and FP input ground motions is adopted here to represent the IM of a motion pair:

$$IM = \sqrt{IM_{FN} \times IM_{FP}} \quad (10)$$

During the analyses, responses of the following components (engineering demand parameters, EDPs) are recorded: (1) curvature of Section 1, φ_{S1} ; (2) curvature of Section 3, φ_{S3} ; (3) bearing displacement between girder and pier $\sigma_{b,pier}$; (4) bearing displacement between girder and pylon $\sigma_{b,pylon}$; (5) force of the longest backstay cable (N121) F_{bc} ; and (6) force of the longest forestay cable (N221) F_{fc} . The upper sides of the pylon are less vulnerable than the lower sides, and the pier has a small effect on the seismic responses of the bridge compared to the pylon [38], so their responses are not considered in this study. Quadratic polynomials are adopted to construct the PSDMs.

Because the regression model is quadratic, the criteria of an optimal IM for linear regressions (practically, efficiency, proficiency, and sufficiency [57]) are not appropriate here. In this study, the determination coefficient (R^2) of the regression is used to judge whether an IM is optimal or not. The definition of R^2 is given as follows:

$$R^2 = \frac{\sum(\hat{y} - \bar{y})^2}{\sum(y - \bar{y})^2} = 1 - \frac{\sum(y - \hat{y})^2}{\sum(y - \bar{y})^2} \quad (11)$$

where y is the sample value, \hat{y} is the regression value, and \bar{y} is the mean of the sample. The larger R^2 , the better the regression is.

Figure 8 plots the determination coefficients for the regressions in the case of each IM candidate. As shown in Figure 8, the largest R^2 varies for different EDPs. Additionally, R^2 can be significantly different for an EDP in different directions. For example, PGV performs well in predicting the transverse bearing displacements, pylon responses, and the backstay cable's force but may not provide reliable predictions on bearing displacements in the longitudinal direction and the force of forestay cables. Therefore, it is difficult to identify the optimal IM from R^2 directly. The multicriteria decision-making (MCDM) method is adopted to tackle this issue. In each MCD, there are several alternatives and criteria. The alternative with the highest score is selected as the best one and is placed in the first rank [58]. In this research, different IMs are considered alternatives, and the corresponding determination coefficients R^2 for different components are chosen as criteria.

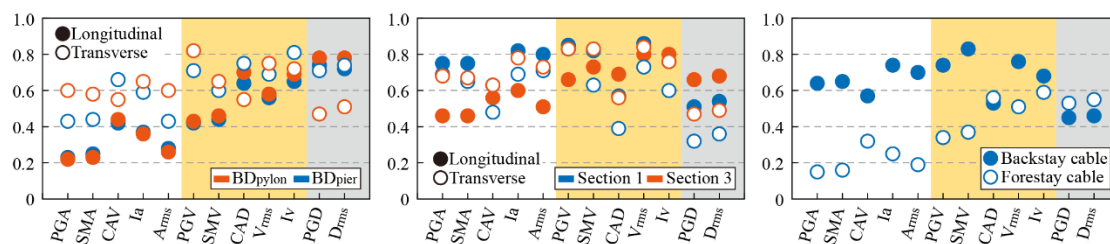


Figure 8. Determination coefficients for the regressions of various EDPs. The background colors denote the type of the IMs (white: acceleration-related; yellow: velocity-related; gray: displacement-related).

The weights of different components are assigned based on 10-point scale qualitative evaluations, as shown in Table 5. Moreover, the weights of a component in different directions are considered to be the same for simplicity. Compared with the bearings, cables and pylons are considered more critical because their failure would cause bridge collapse. As a result, the weights of pylons and cables are both assigned as 10, whereas the weights of bearings are assigned 3, 5, or 7.

Table 5. Assignment of values for a 10-point scale [58].

Attribute Evaluation	Value
Extremely unimportant	0
Very unimportant	1
Unimportant	3
Average	5
Important	7
Very important	9
Extremely important	10

After assigning the weights, a weighted sum method calculates the scores and ranks the IMs. Results of the MCDM method are tabulated in Table 6.

Table 6. Results of the MCDM method.

Weight of Criteria			Rank of the Optimal IMs		
Pylons	Cables	Bearings	1st	2nd	3rd
10	10	7	V_{rms}	I_v	PGV
10	10	5	V_{rms}	I_v	PGV
10	10	3	V_{rms}	I_v	PGV

According to the rank of the IMs for different weight assignments, it is found that V_{rms} is the optimal one among the 12 candidates. Results also demonstrate that the velocity-dependent IMs perform better than the others for all the weight assignments. Moreover, it is worth mentioning that PGA, which has been used as the optimal IM for seismic fragility analyses in previous studies [41,59], is inappropriate for cable-stayed bridges that cross fault ruptures. The PSDMs established for each EDP using V_{rms} are illustrated in Figure 9, and the corresponding regression coefficients are listed in Table 7. It is worth noting that the hazard curve for V_{rms} is unavailable. However, it is possible to establish the correlation between V_{rms} and an IM with available hazard curves, with the development of ground-motion prediction equations, using similar methods introduced in [60].

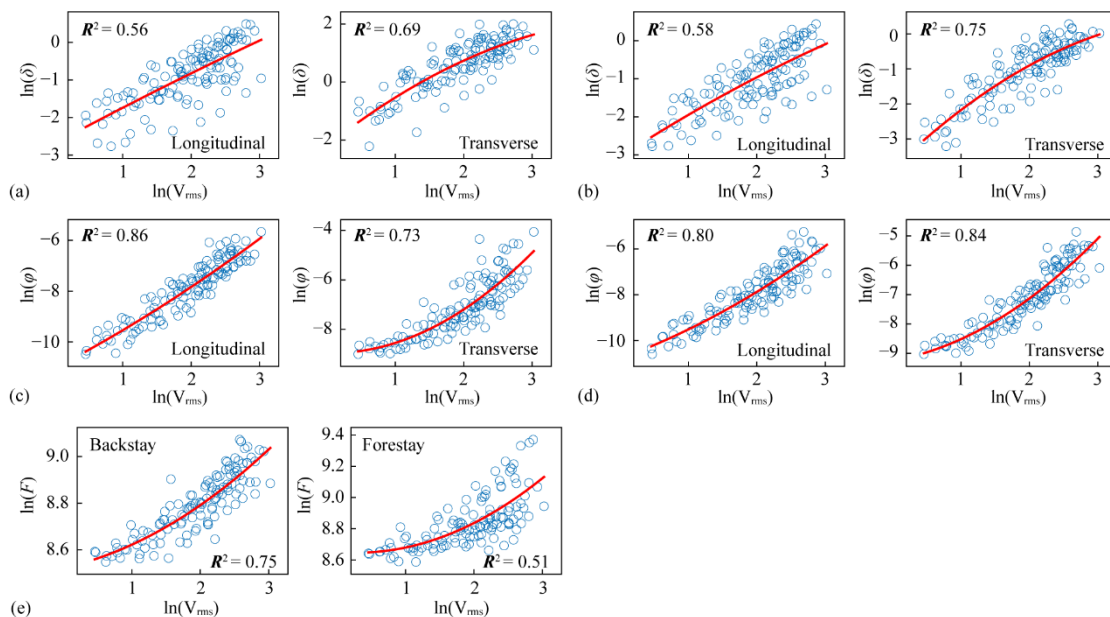


Figure 9. PSDMs for different components: (a) bearing at girder–pier location; (b) bearing at girder–pylon location; (c) Section 1 of the pylon; (d) Section 3 of the pylon; and (e) cables.

Table 7. Regression coefficients for the PSDMs.

EDP	Longitudinal			EDP	Transverse			EDP	/		
	a	b	c		a	b	c		a	b	c
$\sigma_{b, pier}$	-0.022	0.979	-2.696	$\sigma_{b, pier}$	-0.196	1.864	-2.202	F_{bc}	0.035	0.065	8.522
$\sigma_{b, pylon}$	-0.059	1.165	-3.054	$\sigma_{b, pylon}$	-0.203	1.883	-3.856	F_{fc}	0.065	-0.038	8.652
φ_{S1}	0.099	1.408	-11.050	φ_{S1}	0.471	-0.058	-8.963				
φ_{S3}	0.183	1.091	-10.791	φ_{S3}	0.326	0.408	-9.252				

Formulation for the quadratic regression: $\ln(S_D) = a\ln^2(IM) + b\ln(IM) + c$.

4.4. Definition of the Damage Index

Four limit states are considered, namely slight, moderate, extensive, and complete. For the pylon sections, the value of each damage state proposed by Feng [61] is adopted in this study. Figure 10 illustrates the moment-curvature curve for a pylon section. The slight damage state is characterized by the equivalent yield curvature (φ_{ey}), whereas the complete one is characterized by the ultimate curvature (φ_u). Taking the difference between φ_{ey} and φ_u as $\Delta\varphi$, the curvatures that represent moderate and extensive damage states are defined as $(\varphi_{ey} + \Delta\varphi/3)$ and $(\varphi_{ey} + 2\Delta\varphi/3)$, respectively. For the spherical bearings, the slight limit state is defined to be the maximum allowable bearing displacement under normal service conditions; the distance between the center of the bearing and the edge of the masonry plate is defined as the threshold of the extensive damage state, and the threshold of the moderate damage state is defined as the median of slight and extensive damage states; when the center of the bearing moves over the edge of the substructure (i.e., the cap or cross girder), the bearing is considered to be completely damaged. Figure 11 gives the definition of the damage states for the bearing. For the cable forces, the threshold of the complete damage state is defined as the cable’s breaking force. The difference between the initial and cable-breaking force is quartered, and the quartering points are defined as slight, moderate, and extensive damage thresholds.

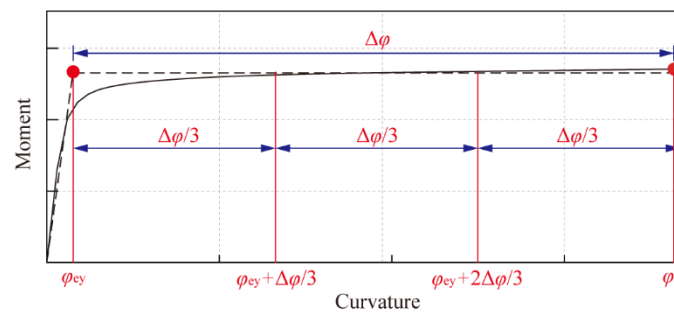


Figure 10. Limit states for the pylons.

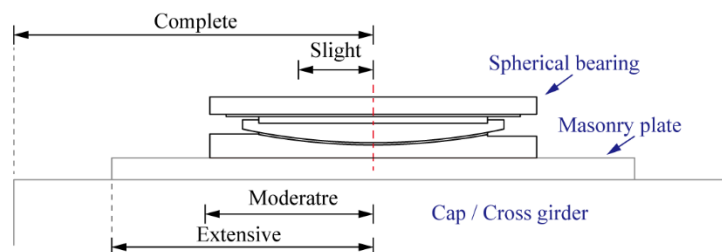


Figure 11. Definition of the damage states for bearings.

Table 8 summarizes the damage index of different damage states for the EDPs, where S_C and β_C mean the median and logarithmic standard deviation, respectively. Note that the thresholds of slight, moderate, and extensive damage states for the bearings are the same in longitudinal and transverse directions. However, the bearing’s complete damage state

threshold is larger in the transverse direction because of the adequate distance between the bearing’s center line and the cap’s transverse edge.

Table 8. Damage index for different damage states.

EDP	Slight		Moderate		Extensive		Complete	
	S_C	β_C	S_C	β_C	S_C	β_C	S_C	β_C
φ_{S1} , longitudinal	1	0.04	6.1	0.05	11.2	0.05	16.3	0.06
φ_{S1} , transverse	1	0.04	7.6	0.04	14.3	0.04	20.9	0.04
φ_{S3} , longitudinal	1	0.15	6.7	0.06	12.5	0.06	18.2	0.06
φ_{S3} , transverse	1	0.13	7.1	0.04	13.2	0.04	19.3	0.04
σ_b , longitudinal (mm)	300	0.35	450	0.35	600	0.35	800	0.35
σ_b , transverse (mm)	300	0.35	450	0.35	600	0.35	2500	0.35
F_{bc} (kN)	8586	0.10	11,785	0.10	14,987	0.10	18,188	0.10
F_{fc} (kN)	8279	0.10	11,196	0.10	14,114	0.10	17,031	0.10

β_C for bearing displacements and cable forces refers to [13].

4.5. Component Fragility Curves

Utilizing the aforementioned PSDMs, the component fragility curves for the fault-crossing bridge under different limit states are developed, as presented in Figure 12. As shown in Figure 12, the bearings at girder–pier locations are the most fragile components for all damage states, especially in the transverse direction. Comparing the bearings at different locations, their vulnerabilities are similar in the longitudinal direction but different in the transverse direction. This can be attributed to the rotation of the deck caused by the permanent displacement.

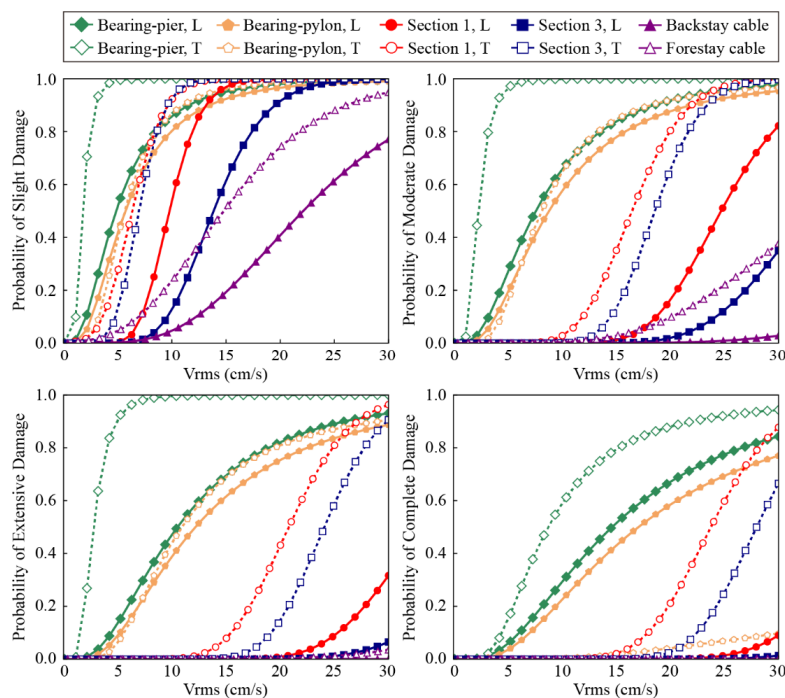


Figure 12. Component fragility curves for the fault-crossing bridge.

Figure 12 also shows that the pylon sections are more vulnerable in the transverse direction, and the pylon bottom section (Section 1) is more vulnerable than the section of the connection zone between the pylon and lower cross-girder (Section 3). Although the capacity of Section 1 is stronger than that of Section 3 (as shown in Figure 4), the pylon bottom can suffer larger seismic forces under earthquakes, which results in its higher vulnerability.

As for the cables, they are likely to experience only slight and moderate damage. Furthermore, the forestay one appears more vulnerable than the backstay one. This is because the girder’s inertia force is undertaken alone by the forestay cables in the middle span and the backstay cables and transition piers in the side span.

5. Comparison of the Fragility of the Bridge Subjected to Fling-Step and Near-Faults Motions

To investigate the influence of traversing a fault rupture on the vulnerability of cable-stayed bridges, fragility curves of the same case bridge near the fault rupture are developed as a comparison. The finite element model, input ground motions, selected IM, and EDPs are the same as those described in previous sections. The only difference is that the transverse excitations are applied to the bridge with equal amplitudes and the same polarity for the near-fault scenario, as shown in Figure 13.

Figure 14 compares the component fragility curves of the bridge subjected to near-fault and fling-step motions. Fragility curves of the cables under extensive and complete damage states are not plotted because of their low damage-exceedance probabilities. Table 9 presents the median value (the V_{rms} associated with the 50% exceedance probability) of the fragility curves across the four limit states. Note that a larger median V_{rms} means the component is less vulnerable.

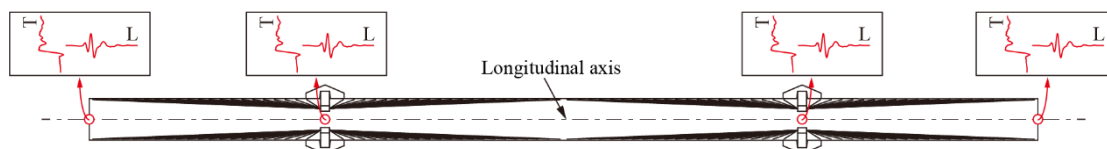


Figure 13. Input ground motions for near-fault cable-stayed bridges.

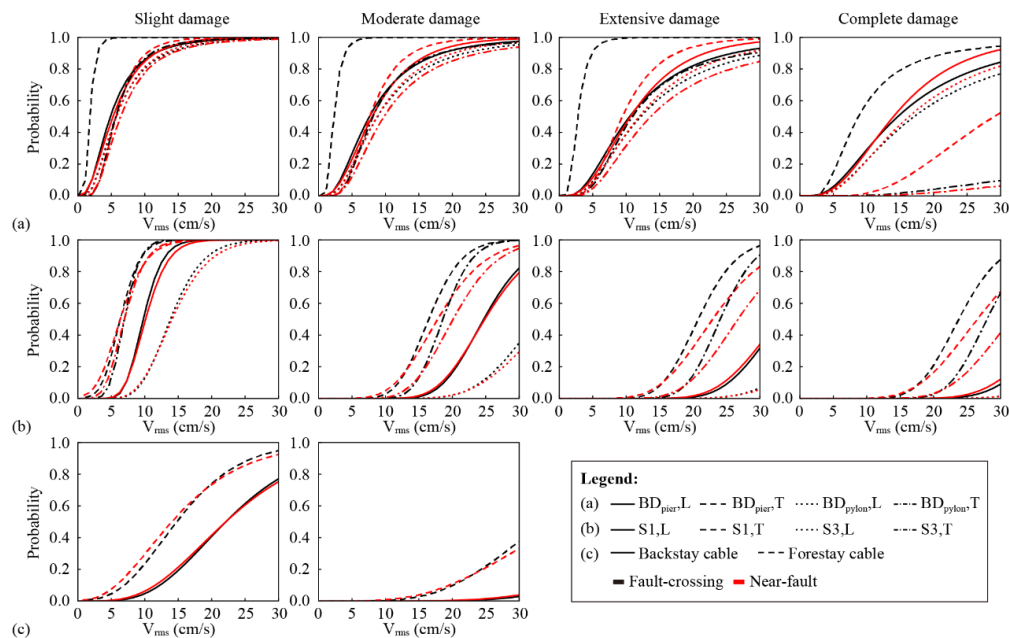


Figure 14. Comparison between the component fragility curves of fault-crossing and near-fault cable-stayed bridges for (a) bearings, (b) pylons, and (c) cables.

Table 9. Median V_{rms} across different damage states for fault-crossing and near-fault bridges (unit: cm/s).

EDP	Slight		Moderate		Extensive		Complete	
	FC	NF	FC	NF	FC	NF	FC	NF
$\sigma_{b,pier}$, longitudinal	4.86	5.24	7.62	8.00	10.56	10.63	14.71	13.95
$\sigma_{b,pier}$, transverse	1.77	5.70	2.28	7.63	2.76	9.43	8.73	29.02
$\sigma_{b,pylon}$, longitudinal	5.71	5.75	8.81	8.76	12.17	11.90	17.08	16.27
$\sigma_{b,pylon}$, transverse	5.65	6.37	8.15	9.76	10.97	13.62	/	/
φ_{S1} , longitudinal	9.77	10.12	24.67	24.88	33.08	32.93	39.49	38.97
φ_{S1} , transverse	6.34	6.33	16.45	17.80	20.76	22.91	23.72	26.49
φ_{S3} , longitudinal	13.85	14.12	32.82	34.64	42.35	45.30	49.31	53.18
φ_{S3} , transverse	6.96	6.96	18.61	20.13	24.10	26.75	28.00	31.57
F_{bc}	22.04	21.73	59.95	59.08	/	/	/	/
F_{fc}	14.80	14.02	33.76	36.57	/	/	/	/

Figure 14a depicts that the transverse vulnerability of the bearings at the girder–pier location is significantly different for the two scenarios. Bearings at that location are much more vulnerable to fault-crossing cable-stayed bridges due to the deck’s rotation, which is, as mentioned earlier, caused by permanent ground dislocations. As presented in Table 9, the median root-mean-square velocities of the bearings’ longitudinal vulnerabilities are similar for the two case bridges. However, Figure 14a shows that when the intensity of ground motions is high, bearings of the bridge subjected to near-fault motions are a little more vulnerable in the longitudinal direction.

Figure 14b compares the vulnerabilities of the pylons for fault-crossing and near-fault bridges. It illustrates that the pylon’s vulnerabilities for the two scenarios are comparable under the slight damage state. However, the pylon’s transverse vulnerabilities of fault-crossing bridges become higher under the other three damage states, whereas its longitudinal vulnerabilities remain comparable. According to Table 9, the median root-mean-square velocities of the transverse moderate, extensive, and complete damage states of Section 1 for near-fault bridges are 8%, 10%, and 12% larger than those for fault-crossing bridges. Similarly, differences in median values of these damage states of Section 3 between the two cases are 8%, 11%, and 13%, respectively. This is because the transverse seismic responses of the pylon for the fling-step bridge contain not only dynamic ones but also static ones exerted by the ground dislocation. Thus, the transverse seismic demand of the pylon for fault-crossing bridges can be more significant than that for near-fault bridges. In other words, there is a high risk of suffering severe damages in the transverse direction for the pylons if the bridge crosses a fault.

Figure 14c and Table 9 show that the vulnerabilities of the stay cables are almost the same under slight and moderate damage states, whether the bridge is across a fault rupture or not. Such phenomena can be attributed to the fact that the cable force is mainly affected by the vertical and longitudinal deformations of the girder and pylons, and these deformations of the near-fault bridges are supposed to be similar to those of the fault-crossing bridges.

6. Conclusions

This study aims at the seismic fragility assessment for cable-stayed bridges crossing faults. Synthetic fling-step motions are generated and applied to the numerical models. The optimal ground-motion intensity measure for the bridge is identified among 12 candidates. Fragility analysis is conducted, and the results are compared. The conclusions are summarized as follows:

- (1) According to the coefficient of determination R^2 and the multicriteria decision-making (MCDM) method, the root-mean-square velocity (V_{rms}) is identified as the optimal IM for the cable-stayed bridge crossing faults.
- (2) Bearings are the most fragile components for the fault-crossing bridge, especially in the transverse direction of those on transition piers. The pylon bottom is more

- vulnerable than the connection zone between the pylon and cross-girder. In contrast, the cables are not likely to suffer severe damage.
- (3) Compared with the bridge subjected to near-fault motions, the vulnerability of pylons and bearings of the fault-crossing bridge becomes higher in the transverse direction. However, the vulnerability of the cables is comparable.
 - (4) This study limits the fragility analysis of cable-stayed bridges subjected to vertical strike-slip faults with a fault crossing angle of 90° . The vulnerability of cable-stayed bridges crossing dip-slip and oblique-slip faults or existing bridges with other fault crossing angles needs further investigation.

Author Contributions: Conceptualization, J.G., Y.G., W.W., S.C. and X.D.; methodology, J.G., Y.G.; investigation, W.W. and X.D.; writing—original draft preparation, J.G. and Y.G.; writing—review and editing, S.C. and X.D.; supervision, X.D.; formal analysis, J.G. and Y.G.; validation, W.W. and X.D. All authors have read and agreed to the published version of the manuscript.

Funding: This research was funded by the National Key Research and Development Program of China (2019YFE0112300); The Shanghai Post-doctoral Excellent Program (2021333); The Post-doctoral Innovation Practice Base Program of Shanghai Yangpu District; and the National Natural Science Foundation of China (51978512).

Conflicts of Interest: The authors declare no conflict of interest.

References

1. Hui, Y.; Wang, K.; Wu, G.; Li, C. Seismic responses of bridges crossing faults and their best crossing angles. *J. Vib. Shock* **2015**, *34*, 6–11. (In Chinese)
2. Yang, S.; Mavroeidis, G.P. Bridges crossing fault rupture zones: A review. *Soil Dyn. Earthq. Eng.* **2018**, *113*, 545–571. [[CrossRef](#)]
3. Yang, S.; Mavroeidis, G.P.; Tsopelas, P. Seismic response study of ordinary and isolated bridges crossing strike-slip fault rupture zones. *Earthq. Eng. Struct. Dyn.* **2021**, *50*, 2841–2862. [[CrossRef](#)]
4. Park, S.W.; Ghasemi, H.; Shen, J.; Somerville, P.G.; Yen, W.P.; Yashinsky, M. Simulation of the seismic performance of the Bolu Viaduct subjected to near-fault ground motions. *Earthq. Eng. Struct. Dyn.* **2004**, *33*, 1249–1270. [[CrossRef](#)]
5. Goel, R.K.; Asce, F.; Chopra, A.K.; Asce, M. Role of Shear Keys in Seismic Behavior of Bridges Crossing Fault-Rupture Zones. *J. Bridg. Eng.* **2008**, *13*, 398–408. [[CrossRef](#)]
6. Goel, R.K.; Chopra, A.K. Nonlinear analysis of ordinary bridges crossing fault-rupture zones. *J. Bridg. Eng.* **2009**, *14*, 216–224. [[CrossRef](#)]
7. Goel, R.K.; Chopra, A.K. Linear analysis of ordinary bridges crossing fault-rupture zones. *J. Bridg. Eng.* **2009**, *14*, 203–215. [[CrossRef](#)]
8. Ucak, A.; Mavroeidis, G.P.; Tsopelas, P. Assessment of Fault Crossing Effects on a Seismically Isolated Multi-Span Bridge. In Proceedings of the 15th World Conference on Earthquake Engineering (15WCEE), Lisbon, Portugal, 24–28 September 2012.
9. Ucak, A.; Mavroeidis, G.P.; Tsopelas, P. Behavior of a seismically isolated bridge crossing a fault rupture zone. *Soil Dyn. Earthq. Eng.* **2014**, *57*, 164–178. [[CrossRef](#)]
10. Yang, H.; Li, J. Response analysis of seismic isolated bridge under influence of fault-crossing ground motions. *J. Tongji Univ. (Nat. Sci.)* **2015**, *43*, 1144–1152. (In Chinese) [[CrossRef](#)]
11. Zhang, F.; Li, S.; Wang, J.; Zhang, J. Effects of fault rupture on seismic responses of fault-crossing simply-supported highway bridges. *Eng. Struct.* **2020**, *206*, 110104. [[CrossRef](#)]
12. Sharabash, A.M.; Andrawes, B.O. Application of shape memory alloy dampers in the seismic control of cable-stayed bridges. *Eng. Struct.* **2009**, *31*, 607–616. [[CrossRef](#)]
13. Zhong, J.; Jeon, J.-S.; Yuan, W.; DesRoches, R. Impact of Spatial Variability Parameters on Seismic Fragilities of a Cable-Stayed Bridge Subjected to Differential Support Motions. *J. Bridg. Eng.* **2017**, *22*, 04017013. [[CrossRef](#)]
14. Zeng, C.; Song, G.; Jiang, H.; Huang, L.; Guo, H.; Ma, X. Nonlinear Seismic Response Characteristics of Fault-crossing Single-tower Cable-stayed Bridge. *China J. Highw. Transp.* **2021**, *34*, 230–245. (In Chinese)
15. Gu, Y.; Guo, J.; Dang, X.; Yuan, W. Seismic performance of a cable-stayed bridge crossing strike-slip faults. *Structures* **2022**, *35*, 289–302. [[CrossRef](#)]
16. Wu, Y.M.; Wu, C.F. Approximate recovery of coseismic deformation from Taiwan strong-motion records. *J. Seismol.* **2007**, *11*, 159–170. [[CrossRef](#)]
17. Iwan, W.D.; Moser, M.A.; Peng, C.-Y. Some observations on strong-motion earthquake measurement using a digital accelerograph. *Bull. Seismol. Soc. Am.* **1985**, *75*, 1225–1246. [[CrossRef](#)]
18. Boore, D.M. Effect of baseline corrections on displacements and response spectra for several recordings of the 1999 Chi-Chi, Taiwan, earthquake. *Bull. Seismol. Soc. Am.* **2001**, *91*, 1199–1211. [[CrossRef](#)]
19. Lin, Y.; Zong, Z.; Tian, S.; Lin, J. A new baseline correction method for near-fault strong-motion records based on the target final displacement. *Soil Dyn. Earthq. Eng.* **2018**, *114*, 27–37. [[CrossRef](#)]

20. Charles, M. An Analytical Model for Near-Fault Ground Motions and the Response of SDOF Systems. In Proceedings of the 7th U.S. National Conference on Earthquake Engineering, Boston, MA, USA, 21–25 July 2002.
21. Mavroeidis, G.P.; Papageorgiou, A.S. A mathematical representation of near-fault ground motions. *Bull. Seismol. Soc. Am.* **2003**, *93*, 1099–1131. [[CrossRef](#)]
22. Makris, N.; Black, C.J. Dimensional Analysis of Rigid-Plastic and Elastoplastic Structures under Pulse-Type Excitations. *J. Eng. Mech.* **2004**, *130*, 1006–1018. [[CrossRef](#)]
23. Hoseini Vaez, S.R.; Sharbatdar, M.K.; Ghodrati Amiri, G.; Naderpour, H.; Kheyroddin, A. Dominant pulse simulation of near fault ground motions. *Earthq. Eng. Eng. Vib.* **2013**, *12*, 267–278. [[CrossRef](#)]
24. Kamai, R.; Abrahamson, N.; Graves, R. Adding fling effects to processed ground-motion time histories. *Bull. Seismol. Soc. Am.* **2014**, *104*, 1914–1929. [[CrossRef](#)]
25. Burks, L.S.; Baker, J.W. A predictive model for fling-step in near-fault ground motions based on recordings and simulations. *Soil Dyn. Earthq. Eng.* **2016**, *80*, 119–126. [[CrossRef](#)]
26. Yadav, K.K.; Gupta, V.K. Near-fault fling-step ground motions: Characteristics and simulation. *Soil Dyn. Earthq. Eng.* **2017**, *101*, 90–104. [[CrossRef](#)]
27. Hamidi, H.; Khosravi, H.; Soleimani, R. Fling-step ground motions simulation using theoretical-based Green’s function technique for structural analysis. *Soil Dyn. Earthq. Eng.* **2018**, *115*, 232–245. [[CrossRef](#)]
28. Yang, S.; Mavroeidis, G.P.; Ucak, A. Analysis of bridge structures crossing strike-slip fault rupture zones: A simple method for generating across-fault seismic ground motions. *Earthq. Eng. Struct. Dyn.* **2020**, *49*, 1281–1307. [[CrossRef](#)]
29. Papageorgiou, A.S.; Aki, K. A specific barrier model for the quantitative description of inhomogenous faulting and the prediction of strong ground motion. *Bull. Seismol. Soc. Am.* **1983**, *73*, 693–722. [[CrossRef](#)]
30. Rezaeian, S.; Kiureghian, A. Der A stochastic ground motion model with separable temporal and spectral nonstationarities. *Earthq. Eng. Struct. Dyn.* **2008**, *37*, 1565–1584. [[CrossRef](#)]
31. Rezaeian, S.; Kiureghian, A. Der Simulation of synthetic ground motions for specified earthquake and site characteristics. *Earthq. Eng. Struct. Dyn.* **2010**, *39*, 1155–1180. [[CrossRef](#)]
32. Dabaghi, M.; Der Kiureghian, A. *Stochastic Modeling and Simulation of Near-Fault Ground Motions for Performance-Based Earthquake Engineering*; University of California: Berkeley, CA, USA, 2014.
33. Dabaghi, M.; Der Kiureghian, A. Stochastic model for simulation of near-fault ground motions. *Earthq. Eng. Struct. Dyn.* **2016**, *46*, 963–984. [[CrossRef](#)]
34. Dabaghi, M.; Der Kiureghian, A. Simulation of orthogonal horizontal components of near-fault ground motion for specified earthquake source and site characteristics. *Earthq. Eng. Struct. Dyn.* **2018**, *47*, 1369–1393. [[CrossRef](#)]
35. Pang, Y.; Wu, X.; Shen, G.; Yuan, W. Seismic Fragility Analysis of Cable-Stayed Bridges Considering Different Sources of Uncertainties. *J. Bridg. Eng.* **2014**, *19*, 04013015. [[CrossRef](#)]
36. Zhong, J.; Pang, Y.; Jeon, J.S.; Desroches, R.; Yuan, W. Seismic fragility assessment of long-span cable-stayed bridges in China. *Adv. Struct. Eng.* **2016**, *19*, 1797–1812. [[CrossRef](#)]
37. Zhong, J.; Jeon, J.S.; Ren, W.X. Risk assessment for a long-span cable-stayed bridge subjected to multiple support excitations. *Eng. Struct.* **2018**, *176*, 220–230. [[CrossRef](#)]
38. Zhong, J.; Jeon, J.-S.; Shao, Y.-H.; Chen, L. Optimal Intensity Measures in Probabilistic Seismic Demand Models of Cable-Stayed Bridges Subjected to Pulse-Like Ground Motions. *J. Bridg. Eng.* **2019**, *24*, 04018118. [[CrossRef](#)]
39. Wu, W.; Li, L.; Shao, X. Seismic Assessment of Medium-Span Concrete Cable-Stayed Bridges Using the Component and System Fragility Functions. *J. Bridg. Eng.* **2016**, *21*, 04016027. [[CrossRef](#)]
40. Wang, J.; Li, S.; Zhang, F. Seismic fragility analyses of long-span cable-stayed bridge isolated by SMA Wire-based Smart Rubber Bearing in near-fault regions. *China J. Highw. Transp.* **2017**, *30*, 30–39. (In Chinese) [[CrossRef](#)]
41. Li, C.; Li, H.N.; Hao, H.; Bi, K.; Chen, B. Seismic fragility analyses of sea-crossing cable-stayed bridges subjected to multi-support ground motions on offshore sites. *Eng. Struct.* **2018**, *165*, 441–456. [[CrossRef](#)]
42. Wei, B.; Hu, Z.; He, X.; Jiang, L. Evaluation of optimal ground motion intensity measures and seismic fragility analysis of a multi-pylon cable-stayed bridge with super-high piers in Mountainous Areas. *Soil Dyn. Earthq. Eng.* **2020**, *129*, 105945. [[CrossRef](#)]
43. Zhu, M.; McKenna, F.; Scott, M.H. OpenSeesPy: Python library for the OpenSees finite element framework. *SoftwareX* **2018**, *7*, 6–11. [[CrossRef](#)]
44. Mangalathu, S.; Jeon, J.-S.; Padgett, J.E.; DesRoches, R. Performance-based grouping methods of bridge classes for regional seismic risk assessment: Application of ANOVA, ANCOVA, and non-parametric approaches. *Earthq. Eng. Struct. Dyn.* **2017**, *46*, 2587–2602. [[CrossRef](#)]
45. Pan, Y.; Agrawal, A.K.; Ghosn, M. Seismic Fragility of Continuous Steel Highway Bridges in New York State. *J. Bridg. Eng.* **2007**, *12*, 689–699. [[CrossRef](#)]
46. Baker, J.W. Quantitative classification of near-fault ground motions using wavelet analysis. *Bull. Seismol. Soc. Am.* **2007**, *97*, 1486–1501. [[CrossRef](#)]
47. Somerville, P.G.; Smith, N.F.; Graves, R.W.; Abrahamson, N.A. Modification of empirical strong ground motion attenuation relations to include the amplitude and duration effects of rupture directivity. *Seismol. Res. Lett.* **1997**, *68*, 199–222. [[CrossRef](#)]
48. Abrahamson, N. Velocity pulses in near-fault ground motions. In Proceedings of the UC Berkeley—CUREE Symposium in Honor of Ray Clough and Joseph Penzien, Berkeley, CA, USA, 9–11 May 2002; pp. 40–41.

49. Guo, J.; Yuan, W.; Dang, X.; Alam, M.S. Cable force optimization of a curved cable-stayed bridge with combined simulated annealing method and cubic B-Spline interpolation curves. *Eng. Struct.* **2019**, *201*, 109813. [[CrossRef](#)]
50. Stefanidou, S.P.; Kappos, A.J. Methodology for the development of bridge-specific fragility curves. *Earthq. Eng. Struct. Dyn.* **2017**, *46*, 73–93. [[CrossRef](#)]
51. Nielson, B.G.; DesRoches, R. Analytical seismic fragility curves for typical bridges in the central and southeastern United States. *Earthq. Spectra* **2007**, *23*, 615–633. [[CrossRef](#)]
52. Wang, X.; Shafieezadeh, A.; Ye, A. Optimal intensity measures for probabilistic seismic demand modeling of extended pile-shaft-supported bridges in liquefied and laterally spreading ground. *Bull. Earthq. Eng.* **2018**, *16*, 229–257. [[CrossRef](#)]
53. Dreger, D.; Hurtado, G.; Chopra, A.; Larsen, S. *Near-Fault Seismic Ground Motions*; Report No. UCB/EERC-2007/03; Earthquake Engineering Research Center, University of California: Berkeley, CA, USA, 2007.
54. Nuttli, O.W. *The Relation of Sustained Maximum Acceleration and Velocity to Earthquake Intensity and Magnitude*; Report No. S-73-1; U.S. Army Engineer Waterways Experiment Station: Vicksburg, MI, USA, 1979.
55. Reed, J.W.; Kassawara, R.P. A criterion for determining exceedance of the operating basis earthquake. *Nucl. Eng. Des.* **1990**, *123*, 387–396. [[CrossRef](#)]
56. Arias, A. *A Measure of Earthquake Intensity*; MIT Press: Cambridge, MA, USA, 1969.
57. Padgett, J.E.; Nielson, B.G.; Desroches, R. Selection of optimal intensity measures in probabilistic seismic demand models of highway bridge portfolios. *Earthq. Eng. Struct. Dyn.* **2008**, *37*, 711–725. [[CrossRef](#)]
58. Hedayati Dezfuli, F.; Alam, M.S. Multi-criteria optimization and seismic performance assessment of carbon FRP-based elastomeric isolator. *Eng. Struct.* **2013**, *49*, 525–540. [[CrossRef](#)]
59. Zhang, C.; Lu, J.; Zhou, Z.; Yan, X.; Xu, L.; Lin, J. Lateral seismic fragility assessment of cable-stayed bridge with diamond-shaped concrete pylons. *Shock Vib.* **2021**, *2021*, 2847603. [[CrossRef](#)]
60. Bradley, B.A. Empirical correlations between cumulative absolute velocity and amplitude-based ground motion intensity measures. *Earthq. Spectra* **2012**, *28*, 37–54. [[CrossRef](#)]
61. Feng, R.; Yuan, W.; Sextos, A. Probabilistic loss assessment of curved bridges considering the effect of ground motion directionality. *Earthq. Eng. Struct. Dyn.* **2021**, *50*, 3623–3645. [[CrossRef](#)]